SANDIA REPORT
SAND2011-5799
Unlimited Release
Printed August 2011

Microkinetic Modeling of Lean NO_x Trap Sulfation and Desulfation

Richard S. Larson

Prepared by
Sandia National Laboratories
Albuquerque, New Mexico 87185 and Livermore, California 94550

Sandia National Laboratories is a multi-program laboratory managed and operated by Sandia Corporation, a wholly owned subsidiary of Lockheed Martin Corporation, for the U.S. Department of Energy's National Nuclear Security Administration under contract DE-AC04-94AL85000.

Issued by Sandia National Laboratories, operated for the United States Department of Energy by Sandia Corporation.

Available to DOE and DOE contractors from
U.S. Department of Energy
Office of Scientific and Technical Information
P.O. Box 62
Oak Ridge, TN 37831

Telephone: (865) 576-8401
Facsimile: (865) 576-5728
E-Mail: reports@adonis.osti.gov
Online ordering: http://www.osti.gov/bridge

Available to the public from
U.S. Department of Commerce
National Technical Information Service
5285 Port Royal Rd.
Springfield, VA 22161

Telephone: (800) 553-6847
Facsimile: (703) 605-6900
E-Mail: orders@ntis.fedworld.gov
Online order: http://www.ntis.gov/help/ordermethods.asp?loc=7-4-0#online

SAND2011-5799
Unlimited Release
Printed August 2011

Microkinetic Modeling of Lean NO_x Trap Sulfation and Desulfation

Richard S. Larson
Hydrogen and Combustion Technology Department
Sandia National Laboratories
P.O. Box 969
Livermore, CA 94551-0969

Abstract

A microkinetic reaction sub-mechanism designed to account for the sulfation and desulfation of a commercial lean NO_x trap (LNT) is presented. This set of reactions is appended to a previously developed mechanism for the normal storage and regeneration processes in an LNT in order to provide a comprehensive modeling tool. The reactions describing the storage, release, and reduction of sulfur oxides are patterned after those involving NO_x, but the number of reactions is kept to the minimum necessary to give an adequate simulation of the experimental observations. Values for the kinetic constants are estimated by fitting semi-quantitatively the somewhat limited experimental data, using a transient plug flow reactor code to model the processes occurring in a single monolith channel. Rigorous thermodynamic constraints are imposed in order to ensure that the overall mechanism is consistent both internally and with the known properties of all gas-phase species. The final mechanism is shown to be capable of reproducing the principal aspects of sulfation/desulfation behavior, most notably (a) the essentially complete trapping of SO_2 during normal cycling; (b) the preferential sulfation of NO_x storage sites over oxygen storage sites and the consequent plug-like and diffuse sulfation profiles; (c) the degradation of NO_x storage and reduction (NSR) capability with increasing sulfation level; and (d) the mix of H_2S and SO_2 evolved during desulfation by temperature-programmed reduction.

ACKNOWLEDGMENTS

The author thanks Jae-Soon Choi of Oak Ridge National Laboratory for useful discussions and for supplying experimental data used in this work. This research was funded by the U.S. Department of Energy's Vehicle Technologies Program via sponsors Gurpreet Singh and Ken Howden. Sandia is a multiprogram laboratory operated by Sandia Corporation, a Lockheed Martin Company, for the US DOE's National Nuclear Security Administration under contract number DE-AC04-94AL85000.

CONTENTS

FIGURES

TABLES

1. INTRODUCTION

The potential advantages of the lean NO_x trap (LNT) in meeting stringent emission standards for diesel and lean-burn gasoline engines have been well documented (Roy and Baiker, 2009). Chief among these is the fact that this technology does not require additional chemicals and/or infrastructure, such as the urea system needed for selective catalytic reduction (SCR). However, a principal concern for LNTs is durability, i.e., the ability to perform their function without loss of efficiency over a very large number of storage and regeneration cycles. Performance loss can result from either chemical poisoning or thermal degradation (or both), and these issues are linked in an LNT. The principal source of poisoning is sulfur in the fuel, which leads to the presence of SO_2 in the exhaust. Because sulfates tend to be bound to the NO_x storage phase (typically BaO) more tightly than are nitrites and nitrates (which, in turn, are bound more tightly than the carbonates normally found), they are not removed during normal catalyst regeneration. Obviously, this leads to non-reproducible cycles as the NO_x storage capacity is gradually degraded. Sulfur can also attach itself to the precious metal phase and potentially interfere with the catalytic reactions occurring there, although this sulfidation is probably reversible. In any case, if the LNT is to have a long life, the trapped sulfates must be removed periodically to restore the NO_x storage capacity. This is typically done by subjecting the catalyst to high temperatures in the presence of a reductant such as H_2. Unfortunately, the use of a reductant implies the same kind of fuel penalty associated with normal regeneration, and the high temperatures can lead to degradation via sintering (for example). Thus, the desulfation process must be planned and carried out very carefully in order to restore the catalyst both economically and without damage. Clearly, a thorough understanding of the chemistry involved in both sulfation and desulfation should be helpful in improving and optimizing this facet of LNT operation. The purpose of this paper is to propose a microkinetic (elementary) reaction mechanism that can reproduce observed sulfation/desulfation behavior, thus potentially allowing fundamental improvements to be made.

While the importance of LNT sulfation has long been recognized, and extensive experimental studies have been conducted (Choi et al., 2007; Choi et al., 2008; Choi et al., 2010; Corbos et al., 2008; Dawody et al., 2005; Elbouazzaoui et al., 2005; Engstrom et al., 1999; Happel et al., 2010;

Kim et al., 2006; Luo et al., 2008; Sakamoto et al., 2006; Sedlmair et al., 2002; Toops and Pihl, 2008; Wu et al., 2005), very few detailed modeling efforts have been undertaken. Han et al. (2005) constructed a complex reactor model for desulfation but chose to focus on the heat generation needed to drive the process, so their chemistry involved only reformate combustion rather than reactions describing the desulfation itself. At the other extreme, Dawody et al. (2007) considered only sulfation but did propose a multipart, multistep reaction mechanism. Their work differs from that of the current study in many important ways, such as their use of multiple site types on the NO_x storage medium (two for NO_x and three for sulfur), the inclusion of sulfites rather than just sulfates, the use of some admittedly non-elementary reaction steps, the neglect of CO_2 and therefore carbonates, and the use of thermal rather than chemical regeneration of the NO_x storage sites. More recently, Olsson et al. (2010) presented a fairly detailed kinetic model for both sulfation and desulfation, in addition to storage and reduction of both NO_x and oxygen. However, they used predominantly global and often irreversible reactions, making it impossible to enforce thermodynamic consistency within the mechanism. In addition, their reaction set was not designed to account for the formation of H_2S (which was not monitored in the associated experiments), nor did it include a reverse water-gas shift reaction to account for CO formation during regeneration.

The purpose of the present study, then, was to develop a microkinetic, thermodynamically consistent sub-mechanism describing specifically the processes involved in LNT sulfation and desulfation. This was designed to be appended to the previously developed mechanism for normal LNT cycling (Larson et al., 2011), which was carried over without any modification. The kinetic parameters for the new reactions were estimated by using the complete mechanism to simulate, to the extent feasible, a suite of sulfation and desulfation experiments reported in the literature. As in our previous study, the simulations were carried out with a transient plug flow reactor code under the assumption that mass-transfer resistances were negligible (or could be incorporated into the kinetics). The number of new reactions was kept to the bare minimum due to the relative sparsity of data and the semi-quantitative nature of the fitting. While these limitations perhaps caused the details of the new sub-mechanism to be somewhat uncertain, the model was nevertheless found to be capable of reproducing adequately all of the principal features of sulfation and desulfation behavior.

2. TEST SUITE

Before attempting to construct and optimize a reaction mechanism, it was necessary to select a set of experiments with which the simulations could be compared. A logical choice was the standard protocol described and used by Choi et al. (2007). This had the crucial advantage that it involved the same commercial Umicore catalyst that was used in developing the storage/regeneration mechanism (Larson et al., 2011); were this not true, the previously inferred kinetic constants could not be assumed to be applicable. On the other hand, this protocol involved roughly 300 short NO_x storage/reduction (NSR) cycles, both with and without SO_2 in the feed, and this large number presented a serious computational challenge, given the number of complete sequences that had to be simulated to optimize the kinetic parameters. Another complication was that significant exotherms were observed during the NSR cycles, especially during the rich phase. The simulation of such temperature excursions with sufficient accuracy to be useful was questionable with currently available thermodynamic data and modeling tools.

In order to deal with these challenges, we adopted two simplifications that allowed us to minimize the computational burden while maintaining fidelity with the experiments. The first approximation involved reducing the total number of cycles to be simulated, albeit modestly. Numerical experiments showed that there was no choice but to simulate the sulfation cycles just as in the experimental recipe, because sulfation is an inherently transient process whose outcome depends on both the total elapsed time and the duration of the individual cycles. On the other hand, ordinary NSR cycles are designed to be reproducible, and there is nothing to be gained by simulating them beyond the point at which they become so. Therefore, in our calculations, SO_2-free cycles were simulated not for the full time period specified experimentally, but only for as long as necessary to ensure repeatability.

The second simplification was to forego any attempt to simulate the temperature excursions in the reactor during cycling, and instead to use the temperature reported experimentally as a function of time, axial position, and sulfation level. Because this inevitably involved some interpolation, it could have led to some errors in the kinetic parameters, but it was considered to be the most accurate option available, and it was in any case largely consistent with the approach

taken in Larson et al. (2011). As a check, supplementary calculations were performed using a spatially uniform and time-independent catalyst temperature of 345°C, which was the rough average of the measured outlet values. This was also essentially the average of the highest and lowest temperatures recorded anywhere in the reactor, with excursions of about 20°C in either direction being possible. These computations demonstrated that the simulation results were not very sensitive to the details of the temperature field, although the use of nonuniform temperatures did give a modestly better fit to the data.

The set of experiments that was simulated in order to estimate the kinetic constants was thus as follows:

(1) one ordinary (SO_2-free) NSR cycle with an unsulfated catalyst, previously determined to be repeatable, to establish the baseline NSR performance;

(2) 111 sulfation cycles, comprising the first 2 hr sulfation episode;

(3) 10 ordinary NSR cycles (enough to reach a state of repeatability) to assess the new and presumably degraded NSR performance;

(4) a repeat of (2), representing the second sulfation episode;

(5) a repeat of (3) to assess the NSR performance of the maximally sulfated catalyst (3.4 g S/L);

(6) a desulfation regimen by temperature-programmed reduction according to the recipe shown in Choi et al. (2007), followed by an artificial cooldown period;

(7) a repeat of (3) to assess the NSR performance of the newly desulfated catalyst.

The channel length, channel diameter, and space velocity for all runs were the same as used in Choi et al. (2007): 7.4 cm, 0.119 cm, and 30,000 hr^{-1} (measured at STP), respectively. All inlet gas flows contained 5% H_2O, 5% CO_2, and N_2 as the balance gas. Beyond these commonalities, the conditions for the various kinds of runs were as follows.

For each NSR cycle (ordinary or sulfation), the lean phase had a duration of 60 s and an inlet gas containing 300 ppm NO and 10% O_2. The rich phase lasted for 5 s and used 3.4% H_2 in the feed. For the sulfation cycles, 20 ppm SO_2 was added to both the lean and rich phase feeds. Transitions in the feed composition were spread over an interval of about 0.1 s. The nominal inlet temperature was in all cases 325°C, although actual measured temperatures were higher.

For the desulfation simulation, the feed gas contained 0.1% H_2. The temperature program used was that depicted in Figure 7 of Choi et al. (2007), which differs slightly from the description in the text. Thus, the temperature ramp started at 331°C and had a rate of about 4.53°C/min rather than the nominal 5°C/min, the soak temperature was about 671°C rather than 700°C, and the duration of the soak was about 1.28 h rather than 1 h. The desulfation was followed by an artificial cooldown over a period of about 15 min prior to the final NSR cycling. Spatial variations in temperature during desulfation were neglected, as no data were available, but they were likely unimportant.

3. MECHANISM DEVELOPMENT

As in our previous studies, the first step in constructing the reaction mechanism was to identify an appropriate set of chemical species. In this case, it was necessary only to decide upon the sulfur-containing species, as all others were to be carried over from the storage/regeneration mechanism (Larson et al., 2011). As noted earlier, we were motivated to keep the list of species and reactions as short as possible (while still allowing for a truly microkinetic mechanism), due to the relatively small amount of hard data and the semi-quantitative nature of the fitting process. The three seemingly essential gas-phase species were SO_2 (present in the feed during sulfation), SO_3 (the logical precursor to stored sulfate), and H_2S (the primary desulfation product). There seems to be little evidence in the literature to support the inclusion of COS. The crucial surface species on the precious metal (nominally platinum) sites were the adsorbed forms and subsequent decomposition products of SO_2 and H_2S, namely SO_2(Pt), H_2S(Pt), SO(Pt), S(Pt), and HS(Pt). SO_3(Pt) was initially included as well but was eventually determined not to be useful in interpreting the data. Because there is clear evidence that both NO_x storage (BaO) and oxygen storage (Ce_2O_3) sites are subject to sulfation (Choi et al., 2007), three sulfates denoted as $BaSO_4$, CeO–SO_4, and $Ce(SO_4)_2$ were also included in the list of surface species. The decision to consider only Ce(IV) sulfates was based on simulation results showing that CeO_2 appears to dominate Ce_2O_3 during short NSR cycles, even during the rich phase. Choi et al. (2010) did not observe sulfites of any kind, so they were not considered here, even though they do appear in other models (Dawody et al., 2007; Olsson et al., 2010).

Next, a candidate list of reactions involving the newly-defined species was assembled. This was done largely by analogy with the NO_x mechanism, with the realization that some of the reactions would probably be found to be unimportant during the fitting process. The chosen reactions, all of them reversible, fell into the following categories:

(a) adsorption of gas-phase molecules onto precious metal (Pt) sites;

(b) stepwise decomposition of the adsorbed molecules, entirely on the Pt phase;

(c) reduction and oxidation of the adsorbed molecules by species residing on adjacent Pt sites;

(d) formation of sulfates on BaO sites by either direct deposition of SO_3 or displacement of existing carbonates and nitrates;

(e) formation of sulfates on pre-oxidized BaO sites by deposition of SO_2;
(f) oxidation of SO_2 to SO_3 via reduction of BaO-phase nitrates and peroxides;
(g) oxidation of SO_2 to SO_3 via reaction with oxygen stored on Ce_2O_3;
(h) formation of sulfates on CeO_2 by stepwise deposition of SO_3.
Many other reactions, such as atom transfers between adsorbed NO_2 and SO_2 fragments, could have been proposed, but it is unlikely that any useful kinetic information could have been obtained about them, given their speculative nature and the relative lack of experimental data.

The kinetic constants of the new sulfur-containing reactions in both the forward and reverse directions were regarded as unknown and were therefore determined by the data fitting process. Not all of these parameters were adjusted independently, however, because thermodynamic constraints were in place to ensure consistency with known gas-phase species properties and also between parallel reaction paths, as described elsewhere (Larson et al., 2008) and as detailed below. Additional constraints were imposed in order to ensure that all activation energies were non-negative and both molecular heats of desorption were positive. Finally, the standard centering technique was used to weaken the coupling between the activation energies and the corresponding rate constants, so that the rate constants at a fixed reference temperature (300°C) served as adjustable parameters in place of the pre-exponential factors.

For each candidate mechanism and for each trial set of adjustable parameters, the entire test suite described above was simulated for a single monolith channel with the Chemkin-based transient plug flow reactor code TPLUG (Kee et al., 1999; Larson et al., 2011). This gave a detailed description of both the temporal and axial variations in the channel and thus allowed various experimental observations to be checked. However, it did not include possible radial mass-transfer resistances in the gas and solid (washcoat) phases, so it resulted in a purely kinetic model for the phenomena under study, just as in our previous work.

The adjustment of the kinetic parameters so as to obtain an optimal fit to the experimental data was carried out by the Sandia-developed APPSPACK code (Griffin et al., 2006). This of course required the definition of an objective function that could represent quantitatively the overall quality of the simulation. Due to the complexity of the test suite, we devised a composite

function that would encourage the simulation to satisfy the following five criteria, as suggested by the experimental data. (Full details of the calculation are given in Appendix A.)

(1) The slip of sulfur in any form through the catalyst during sulfation should be minimal.

(2) The sulfation of BaO sites should be plug-like, i.e., the transition between fully sulfated and unsulfated regions should be sharp.

(3) The amounts of H_2S and SO_2 released during desulfation as functions of time should match those observed experimentally.

(4) The desulfation of the catalyst should be nearly complete after the high-temperature soak.

(5) The amounts of NO_x escaping the catalyst during ordinary cycling before sulfation, after each of the two sulfation episodes, and after desulfation should match those observed experimentally.

Because the H_2S and SO_2 concentrations measured during desulfation in Choi et al. (2007) were reported in arbitrary units, it was necessary to scale at least the simulated results in order to compare the two sets. For this purpose, we elected to scale each concentration (measured or simulated) by the appropriate global maximum of the two concentrations, be it H_2S or SO_2. Because this procedure allowed a comparison of only the dimensionless amounts of the two gases, the explicit requirement for complete desulfation was included in order to ensure that absolute amounts were actually being compared.

In evaluating the effect of sulfation on the behavior of the catalyst during ordinary cycling, we elected to look only at the two NO_x species, as the experimental data for the others (e.g., NH_3 and N_2O) was subject to considerable uncertainty due to time lags in the FTIR system. Furthermore, we chose to focus on total NO_x rather than on NO and NO_2 individually, primarily because the former was thought to be less sensitive to uncertainties in the temperature. The integral of the simulated outlet NO_x concentration over the entire cycle was compared to the experimental value inferred from Choi et al. (2007) for each of the four sulfation levels, and the results were combined to construct the 5th contribution to the objective function. It should be noted that no attempt was made to match the time dependence of the NO_x concentration *during* the cycle, so the agreement or lack thereof with the experimental data provided a separate check on the model.

4. FINAL MECHANISM

The sulfation/desulfation mechanism resulting from many iterations of the development process is summarized in Table 1. While this is the principal result of the current study, it can be used only in conjunction with the NO_x storage and reduction mechanism reported previously (Larson et al., 2011), a fact that is emphasized by the reaction numbering. For ease of reference, the base mechanism comprising the first 45 reactions is reproduced in Appendix B.

As suggested earlier, the sulfur reactions occurring on precious metal sites include the adsorption and stepwise decomposition of the gas-phase species SO_2 and H_2S. However, surface reductions of SO_2(Pt) and SO(Pt) were found to be unimportant, as were surface oxidations of H_2S(Pt) and HS(Pt).

The main reaction leading to the formation of sulfates on the BaO phase is simply the deposition of SO_3 on bare oxide sites. Two plausible alternatives, namely the displacement of CO_2 from carbonates and NO_2 from nitrates, in each case by SO_3, were also considered but ultimately rejected as being redundant and insignificant, respectively. However, reaction (S53) provides a sulfation pathway involving the peroxide species BaO–O that plays a prominent role in the NO_x storage process (Larson et al., 2011). The primary contribution of this reaction is to allow $BaSO_4$ formation precisely at the leading edge of the channel. This would otherwise not occur, because there is by assumption no SO_3 in the feed stream.

Of the three reactions describing chemistry on the oxygen storage sites, the sulfation processes (S54) and (S55) are straightforward, but the oxidation process (S56) deserves further comment. Clearly, an oxidation pathway of some sort is needed in order to convert the SO_2 in the inlet gas to the SO_3 that serves as the main sulfation precursor. Two possibilities mentioned above are the reactions of SO_2 with nitrates and peroxides on the BaO phase; however, simulations showed that these processes were ineffective at producing SO_3 in significant amounts. A more conventional pathway would involve the surface oxidation of SO_2(Pt) by O(Pt) and the subsequent desorption of SO_3, by analogy with one of the processes converting NO to NO_2. However, this route was found to be incapable of producing SO_3 at the rate necessary to give

plug-like sulfation of the NO_x storage sites: Rather than being oxidized quickly enough to be deposited at the first available site, the inlet SO_2 tended to survive for some distance downstream, leading to a rather diffuse sulfation front. Presumably, SO_2 was unable to compete for the limited number of Pt sites with NO, which was present at a concentration 15 times greater, and which itself requires an alternate route for oxidation (Larson et al., 2011). By contrast, the ceria phase provides an almost limitless supply of oxidant. In the reverse direction, (S56) simply describes an additional route for oxygen storage on this phase.

The use of (S56) to account for SO_2 oxidation has yet another benefit, in that it allows sulfation to take place even during the rich phase of each short cycle. Unlike O(Pt), which is rapidly consumed after the switch to rich operation, CeO_2 is not severely depleted and thus remains available to oxidize SO_2, thereby preventing the slip of this species from the reactor. Another potential explanation for sulfur trapping during the rich phase is temporary storage on precious metal sites, primarily as S(Pt), but our simulations have shown that the amount stored is not nearly enough to prevent slip from occurring, this likely being a consequence of the relatively small site density of the Pt phase. Still another possibility is that sulfur is stored initially as sulfites, as suggested by Olsson et al. (2010), implying that oxidation of SO_2 is not necessary. However, because no sulfites were observed in the experiments of Choi et al. (2010), we chose not to pursue this option.

One might well ask why (S56) is included when the corresponding reaction involving NO and NO_2 is not. A logical answer is that the oxidation of SO_2 is thermodynamically far more favorable than is that of NO. For a mixture containing 20 ppm of both SO_2 and O_2, the equilibrium conversion to SO_3 at 345°C is 90.1%. However, when the calculation is carried out for NO instead, the conversion to NO_2 is just 3.8%, even if the decomposition to N_2 is ignored. In reality, the decomposition route would dominate and the equilibrium conversion to NO_2 would be negligible. These conclusions remain valid qualitatively even under heavily oxidizing conditions. One could also argue that CO (for example) should be allowed to react with CeO_2, but such a reaction can be assembled from steps appearing in Appendix B, so we have elected not to include this parallel pathway.

It may be noted that Table 1 contains no spillover reactions of the type used in Larson et al. (2011) to describe the reduction of stored NO_x by H(Pt) and CO(Pt). A purely pragmatic reason for this is that, again, such reactions were not helpful in reproducing the data, and leaving them out was consistent with the goal of keeping the mechanism as simple as possible. However, a more compelling reason is that desulfation is generally considered to be a thermally driven event (Han et al., 2005), as is clear from the high temperatures used, whereas the release of NO_x is heavily influenced by a change in the chemical environment. The primary role of the reductant (H_2) used in desulfation is apparently to provide a sink for the released sulfur oxides, thereby preventing the buildup of their concentrations in the reactor and maintaining the driving forces for desorption.

The kinetic parameters listed in Table 1 give the forward and reverse rate constants for each reaction in terms of the generalized Arrhenius expression

$$k = AT^n \exp\left(-E/RT\right) \tag{1}$$

The reactions marked with an asterisk form a complete, linearly independent core set with respect to the sulfur-containing surface species, so the kinetic parameters in both directions were free to vary during the optimization process, although the temperature exponents were set identically to zero. For each of the remaining reactions, the equilibrium constant was subject to a thermodynamic constraint, so the kinetic parameters in only one direction could be varied freely. Kinetic parameters in the other direction were then fixed by the constraint, thus giving rise to a nonzero value of the temperature exponent.

The thermodynamic consistency relations expressing each of the non-core reactions in Table 1 as a linear combination of core gas and surface reactions are as follows:

$$\text{(S50)} = -\text{(G8)} - \text{(S6)} + \text{(S7)} + \text{(S46)} - \text{(S47)} + \text{(S48)} + \text{(S49)} - \text{(S51)} \tag{2}$$

$$\text{(S53)} = \text{(G7)} - 0.5*\text{(S6)} - \text{(S34)} + \text{(S52)} \tag{3}$$

$$\text{(S56)} = \text{(G7)} - 0.5*\text{(S6)} - \text{(S45)} \tag{4}$$

The way in which these equations are translated into relations between the forward and reverse kinetic parameters has been described previously (Larson et al., 2008). The core reactions appearing in these equations include not only some from Table 1, but also a few from Appendix

B as well as two new gas reactions. For convenience, the entire set of gas reactions is listed in Table 2, along with the corresponding equilibrium constants in the form

$$K = K_0 T^n \exp\left(-Q/RT\right) \tag{5}$$

It must be emphasized that none of the gas reactions in Table 2 are actually a part of the overall mechanism. They are introduced solely for the purpose of assuring thermodynamic consistency and play no direct role in the kinetics.

It is easily seen that all of the reactions in Table 1, with the possible exception of (S55), are crucial to reproducing the experimental behavior in its entirety. (S56) provides the only practical means of converting the inlet SO_2 to SO_3, which then leads to sulfate formation via (S52), (S54), and (S55). As noted above, (S53) is necessary to allow sulfation at the leading edge of the channel. Without it, sulfation would still occur almost immediately downstream, due to the rapid oxidation of SO_2; however, the ability to simulate this very sharp transition would be limited by the finite grid spacing, leading to an artificially flawed spatial profile. In any case, reactions (S52)–(S56) are reversed during desulfation, and part of the SO_2 thus produced is converted stepwise to H_2S via (S46), (S48), (S49), (S51), (S50), and (S47) in that order, with the last three of these obviously being run in reverse.

More quantitative information about the roles of the individual reactions can be obtained by computing various kinds of reaction sensitivities. Accordingly, Table 3 shows, for each reaction, the effect on the objective function of increasing or decreasing the forward and reverse rate constants by a factor of 10 or simply deleting the reaction entirely. The entries in the last column basically confirm the discussion of the preceding paragraph, in that none of the reactions can be deleted without significant damage to the overall fit, but that (S53) is the least important in this regard. As expected, a detailed examination shows that the deletion of this reaction is detrimental only because it degrades the plug-like nature of the $BaSO_4$ profile. It is possible that the effect of deleting (S55) could be greatly reduced by altering the rate of (S54) to compensate, but in the optimized mechanism both reactions contribute strongly.

From a purely numerical standpoint, the most crucial reactions in the mechanism are obviously (S54) and (S56). The importance of the latter has already been emphasized, but the results for

(S54) are actually more enlightening. Without this reaction, there can be no sulfation of the oxygen storage sites, so the BaO phase (which has a much smaller site density) becomes completely saturated with $BaSO_4$ throughout the reactor, and its ability to trap NO_x is lost. In addition, a great deal of the incoming SO_2 simply escapes, which further degrades the objective function. It can be concluded that a primary function of the ceria phase in this catalyst is to shield the NO_x storage phase from excessive sulfation, although it is certainly not completely effective at doing so. As evidence of this, Table 3 shows that *increasing* the rates of (S54) and (S55) beyond their established values is also quite detrimental to the fit. Such an increase suppresses the sulfation of BaO sites beyond what actually occurs and causes the amount of NO_x slip during NSR cycling to be underpredicted.

Next, it can be seen that the deletion sensitivities for reactions (S46)–(S51) are all close to one another. This is expected, because these reactions serve only to form a sequence that converts SO_2 to H_2S during desulfation. More interesting is the fact that there are obviously two distinct groups, namely (S46), (S48), and (S49) on the one hand, and (S47), (S50), and (S51) on the other. These two groups allow the conversion of SO_2 to S(Pt) and S(Pt) to H_2S, respectively. The fact that the two deletion sensitivities are unequal implies that S(Pt) is more than just a transitory reaction intermediate, i.e., that it accumulates to a significant extent during desulfation, albeit temporarily. Simulation results to be shown below are in agreement with this, and experimental evidence for the formation of sulfides on Pt under rich conditions has been reported by Sedlmair et al. (2002).

Finally, the rate sensitivities for reactions (S46)–(S51) in Table 3 allow identification of the rate-limiting step(s) in this sequence and imply caveats on the specification of kinetic parameters. Generally, if a substantial increase in the rate of a reaction has no effect, but the deletion of that reaction is detrimental, then it is safe to conclude that the reaction is essentially at equilibrium. It appears that reactions (S47) and (S49)–(S51) (as well as (S53)) fall into this category. For each of these, the forward and reverse rate constants are somewhat uncertain, because they can be increased proportionately (i.e., without changing the equilibrium constant) without affecting the quality of the fit. For such a reaction, the best that can be done is to determine lower bounds for the rate constants, and one can say that these have been found only if a *decrease* in the rate

actually has an effect. In Table 3, this appears to be true for the reactions in question. The two remaining reactions, (S46) and (S48), are clearly not at equilibrium, so they limit (in that order of importance) the rate of conversion of SO_2 to H_2S. Not surprisingly, they are also the first two reactions in the actual sequence.

The foregoing is not meant to imply that reactions (S46)–(S51) function in isolation, for the species O(Pt) and H(Pt) can certainly also participate in many of the reactions listed in Appendix B. It might be argued that the H(Pt) created by adsorption of H_2 during desulfation will drive (S50) and (S51) to the left, thus explaining the rapidity of those reactions. However, much of the H(Pt) will be converted to CO(Pt) by the water-gas shift reaction (S24), and both H(Pt) and CO(Pt) will react quickly with the O(Pt) produced by (S48) and (S49), thereby driving those reactions to the right. Thus, a simple kinetic analysis of the pathway from SO_2 to H_2S is not really possible.

Table 1. Reactions in the sulfation/desulfation submechanism and the corresponding forward and reverse kinetic parameters. An asterisk indicates a core reaction.

No.	Reaction	*A* (cgs units)	*n*	*E* (kJ/mol)
Reactions on precious metal sites:				
(S46)*	$SO_2 + V(Pt) = SO_2(Pt)$	1.882E+08	0	14.47
		6.773E+04	0	17.84
(S47)*	$H_2S + V(Pt) = H_2S(Pt)$	4.944E+10	0	26.56
		1.034E+06	0	26.56
(S48)*	$SO_2(Pt) + V(Pt) = SO(Pt) + O(Pt)$	1.763E+12	0	0.00
		1.399E+21	0	0.96
(S49)*	$SO(Pt) + V(Pt) = S(Pt) + O(Pt)$	9.926E+13	0	30.10
		1.383E+23	0	44.19
(S50)	$H_2S(Pt) + V(Pt) = HS(Pt) + H(Pt)$	1.272E+14	0.8823	76.56
		9.643E+27	0	227.92
(S51)*	$HS(Pt) + V(Pt) = S(Pt) + H(Pt)$	1.254E+15	0	66.26
		1.050E+19	0	116.71
Reactions on NO_x storage sites:				
(S52)*	$SO_3 + BaO = BaSO_4$	1.707E+12	0	32.93
		2.543E+06	0	137.51
(S53)	$BaO–O + SO_2 = BaSO_4$	5.977E+11	0	27.93
		3.118E+04	–0.6738	146.14
Reactions on oxygen storage sites:				
(S54)*	$CeO_2 + SO_3 = CeO–SO_4$	3.585E+06	0	10.15
		3.425E+08	0	175.42
(S55)*	$CeO–SO_4 + SO_3 = Ce(SO_4)_2$	3.579E+06	0	10.15
		2.260E+08	0	175.41
(S56)	$SO_2 + 2CeO_2 = SO_3 + Ce_2O_3$	1.150E+15	0	28.00
		4.147E+13	–0.6738	57.71

Table 2. Gas-phase reactions used in formulating thermodynamic constraints for the overall mechanism.

No.	Reaction	K_0 (cgs units)	n	Q (kJ/mol)
(G1)	$\frac{1}{2}N_2 + \frac{1}{2}O_2 = NO$	3.804E+00	0.0241	90.26
(G2)	$\frac{1}{2}N_2 + O_2 = NO_2$	2.774E–02	0.2472	33.26
(G3)	$CO + \frac{1}{2}O_2 = CO_2$	2.474E–04	0.4874	–283.57
(G4)	$H_2 + \frac{1}{2}O_2 = H_2O$	7.817E+01	–0.623	–239.13
(G5)	$N_2 + \frac{1}{2}O_2 = N_2O$	3.443E–04	0.6574	81.06
(G6)	$\frac{1}{2}N_2 + \frac{3}{2}H_2 = NH_3$	9.381E+01	–0.8361	–42.12
(G7)	$SO_2 + \frac{1}{2}O_2 = SO_3$	2.967E-05	0.6738	–99.84
(G8)	$H_2 + SO_2 = H_2S + O_2$	1.812E+04	–0.8823	278.68

Table 3. Percent increases in the objective function resulting from the speedup or slowdown (each by a factor of 10) or deletion of individual reactions in the mechanism.

Reaction	Speedup	Slowdown	Deletion
(S46)	30.8	197.5	234.1
(S47)	0.0	0.2	218.3
(S48)	0.5	8.5	234.1
(S49)	0.1	0.1	234.1
(S50)	0.0	0.1	218.3
(S51)	0.0	0.1	218.3
(S52)	1.1	2.6	997.2
(S53)	0.0	8.6	17.0
(S54)	959.8	9120.0	9249.4
(S55)	742.9	1300.9	1707.1
(S56)	74.4	804.7	9829.9

5. SIMULATION RESULTS AND DISCUSSION

Some highlights of the simulation of the test suite using the optimized reaction mechanism will now be presented. Figure 1 shows the amounts of sulfur trapped on the catalyst as $BaSO_4$, as $CeO–SO_4$, as $Ce(SO_4)_2$, and in total (including amounts adsorbed on Pt sites) as functions of time during the two long sulfation episodes. As noted earlier, the gap between the two episodes is occupied by 10 ordinary NSR cycles used for performance evaluation. Clearly, trapping of sulfur is initially preferred on the BaO (NO_x storage) sites, but rather quickly the rate of this process falls off as sites near the front end of the catalyst become saturated. Much of the SO_3 is then trapped on ceria sites before it can reach the sulfation front on the BaO phase. As a result of the differing site densities, which are 8.846×10^{-7} and 7.450×10^{-6} mol/cm^2 for the BaO and Ce_2O_3 phases, respectively (Larson et al., 2011), the latter phase becomes the primary sink. In any case, the total amount of trapped sulfur increases almost linearly throughout the process, as expected. This suggests that the amount of sulfur escaping the channel is negligible, and this is confirmed by examining the composition of the outlet stream, as shown below. In fact, the total amount of sulfur trapped at the end of the process is computed to be slightly greater than the amount fed to the channel, so the amount escaping is too small to be determined by difference. Finally, it should be noted that there is no loss of sulfate from either of the two storage phases during the NSR performance evaluation cycles, implying that desulfation cannot be made to occur at these temperatures.

The rapid cycling that occurs during the sulfation episodes leads to behavioral details that are not visible in Figure 1. Figure 2 shows the outlet concentration of H_2S and the spatially-averaged concentration of S(Pt) during the last of the 222 short sulfation cycles. The concentrations of all other sulfur-containing species in the gas or on Pt sites are negligible in comparison to these. Clearly, during virtually all of the lean phase (0–60 s), all of the incoming SO_2 must be trapped on BaO and CeO_2, as it does not appear here. However, during the ensuing rich phase, the strongly reducing atmosphere converts some of the SO_2 to H_2S, and this is accompanied by a noticeable presence of sulfur on the Pt sites. Still, the concentration of H_2S in the outlet stream is only 0.007 ppm, and it is even smaller for earlier cycles, so it is valid to state that the slip of sulfur through the channel is negligible.

Figure 3 shows the spatial profiles of the three sulfate species concentrations at the end of the last sulfation cycle. The first feature to notice is that no sulfates are formed on ceria precisely at the entrance to the channel. Again, this is due to the fact that there is no SO_3 in the inlet stream, so reactions (S54) and (S55), unlike (S53), are not operative. Nevertheless, within a short distance downstream, oxidation of SO_2 to SO_3 is sufficient to allow even the ceria phase to become heavily sulfated. (Note that each phase has its own set of site fractions and that the ceria values can be added.) This occurs so quickly, in fact, that the transition zone cannot really be resolved by the finite grid spacing. However, of more interest is the fact that the sulfation of the BaO phase is highly plug-like, in that the transition from a fully sulfated to an unsulfated state occurs over a very small fraction of the channel length. Thus, the optimization process was successful in encouraging this experimentally observed behavior (Choi et al., 2007). On the other hand, the sulfation of ceria sites is clearly not plug-like at all, but this is also consistent with the experiments, which showed that some oxygen storage capacity remained in the nominally sulfated zone. This feature was not incorporated into the objective function, so the simulation results provide some independent support for the model.

The computed concentrations of the sulfur-containing species in the exit gas during desulfation are shown together with the temperature in Figure 4(a) and together with the corresponding experimental data, replotted from Choi et al. (2007), in Figure 4(b). Under these reducing conditions, the amount of SO_3 produced is negligible, peaking at about 0.01 ppm in the simulation. As noted earlier, a quantitative comparison of model vs. experiment for H_2S and SO_2 is not technically possible due to the nature of the data, but such a comparison can be inferred if it is assumed that both SO_2 trapping during sulfation and sulfur release during desulfation were essentially complete in the experiments. In any case, Figure 4(b) shows that the simulation captures the experimental behavior reasonably well, although the simulated peaks are somewhat too wide at the top and too narrow at the bottom. The pronounced shoulder on the right side of the simulated SO_2 trace, which appears to be echoed in the experimental plot, is a strong indication that more than one type of sulfate is being decomposed.

Figure 5 is the desulfation analog of Figure 1, in that it shows the amounts of sulfur contained within the three sulfate species, as well as the total sulfur remaining on the catalyst, as functions of time. The most striking feature is that the amount of $BaSO_4$ actually increases initially and does not begin to decrease until the ceria phase has been largely desulfated. Together, Figures 4(a) and 5 show that the desulfation of CeO_2 is accompanied by large releases of H_2S and SO_2, but it is equally clear from Figure 5 that some of the released sulfur redeposits on the BaO phase (temporarily, of course). The fact that desulfation of the BaO sites requires higher temperatures than is true for CeO_2 is in agreement with the experimental evidence (Choi et al., 2010).

Figure 6 shows the concentrations of the sulfur-containing species on the precious metal (Pt) sites during desulfation. The main conclusion to be drawn here is that, as in the rich phases of the sulfation cycles, S(Pt) is by far the most prevalent of the species pictured. This is consistent with our earlier discussion regarding the deletion sensitivities of Pt reactions in Table 3. In fact, at its peak during desulfation, S(Pt) is the most abundant of all of the species on the Pt sites, with the exception of vacancies. Of course, this does not mean that the other species in Figure 6 are unimportant, because all of them are involved in the pathway that leads from decomposed sulfates to gas-phase H_2S.

Finally, Figure 7 shows the effects of the various levels of sulfation on the NSR performance of the catalyst, specifically the NO_x slip during an ordinary short cycle. For the simulations, the results correspond to the tenth (and last) cycle after sulfation or desulfation, at which point the behavior had stabilized. As in Figure 4(b), the agreement between simulation and experiment is fairly good. Both show a negligible amount of NO_x slip both before sulfation and after desulfation. The main problem with the simulation seems to be the overly gradual rise in the NO_x slip at the lower level of sulfation. This actually causes the integrated NO_x for this case to be overpredicted, even though the spike at the lean/rich transition is slightly underpredicted. The simulated and experimental results also differ at both levels of sulfation in the amount of detail seen just after the lean/rich transition. However, it is possible that the smoother behavior seen in the experimental results is a consequence of instrument response time limitations.

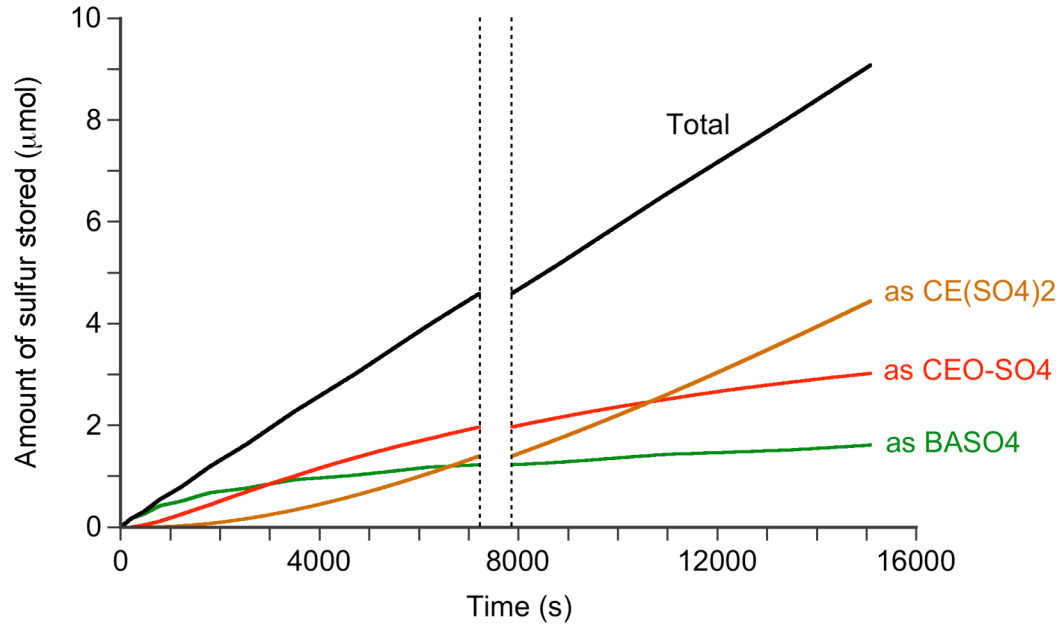

Figure 1. Accumulation of individual sulfate species and total trapped sulfur during sulfation cycles.

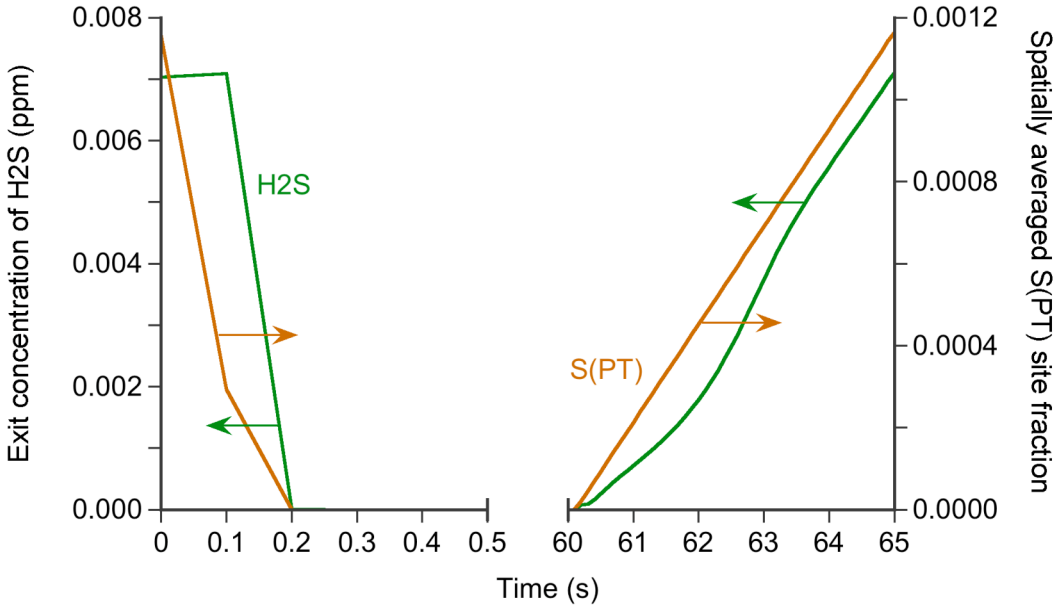

Figure 2. Outlet concentration of H_2S and spatially-averaged concentration of S(Pt) during final sulfation cycle. Concentrations are negligible during the time period not shown.

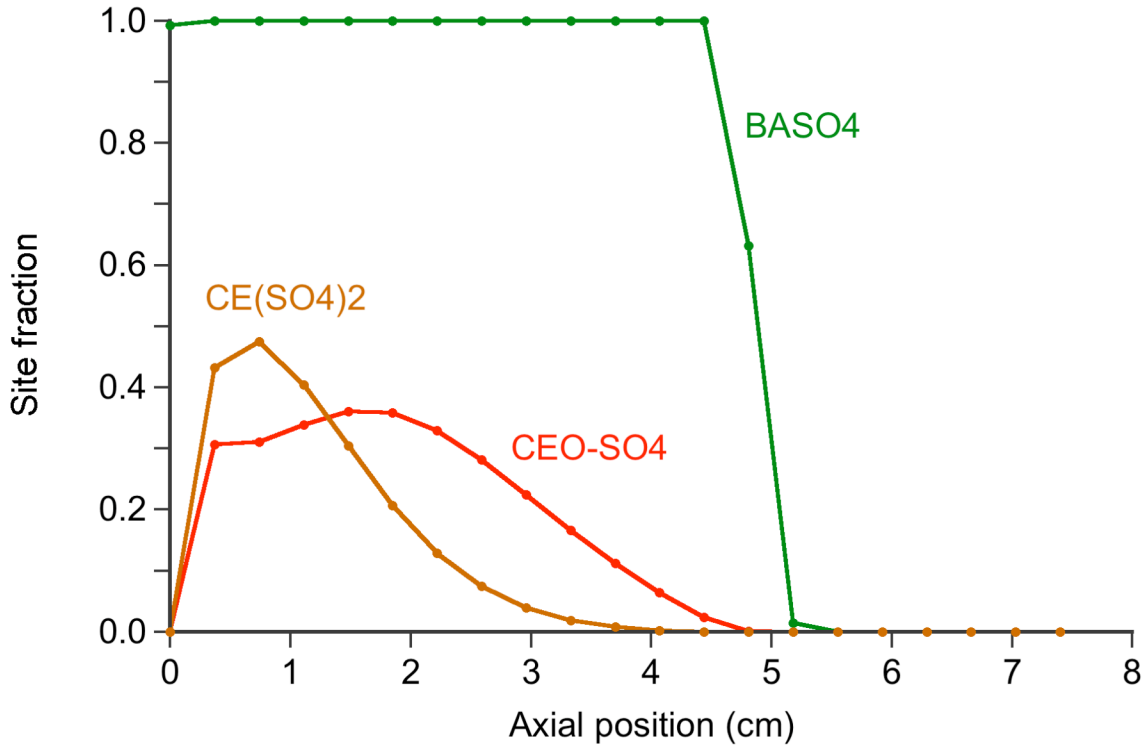

Figure 3. Simulated axial concentration profiles of sulfate species on BaO and CeO_2 at end of final sulfation cycle.

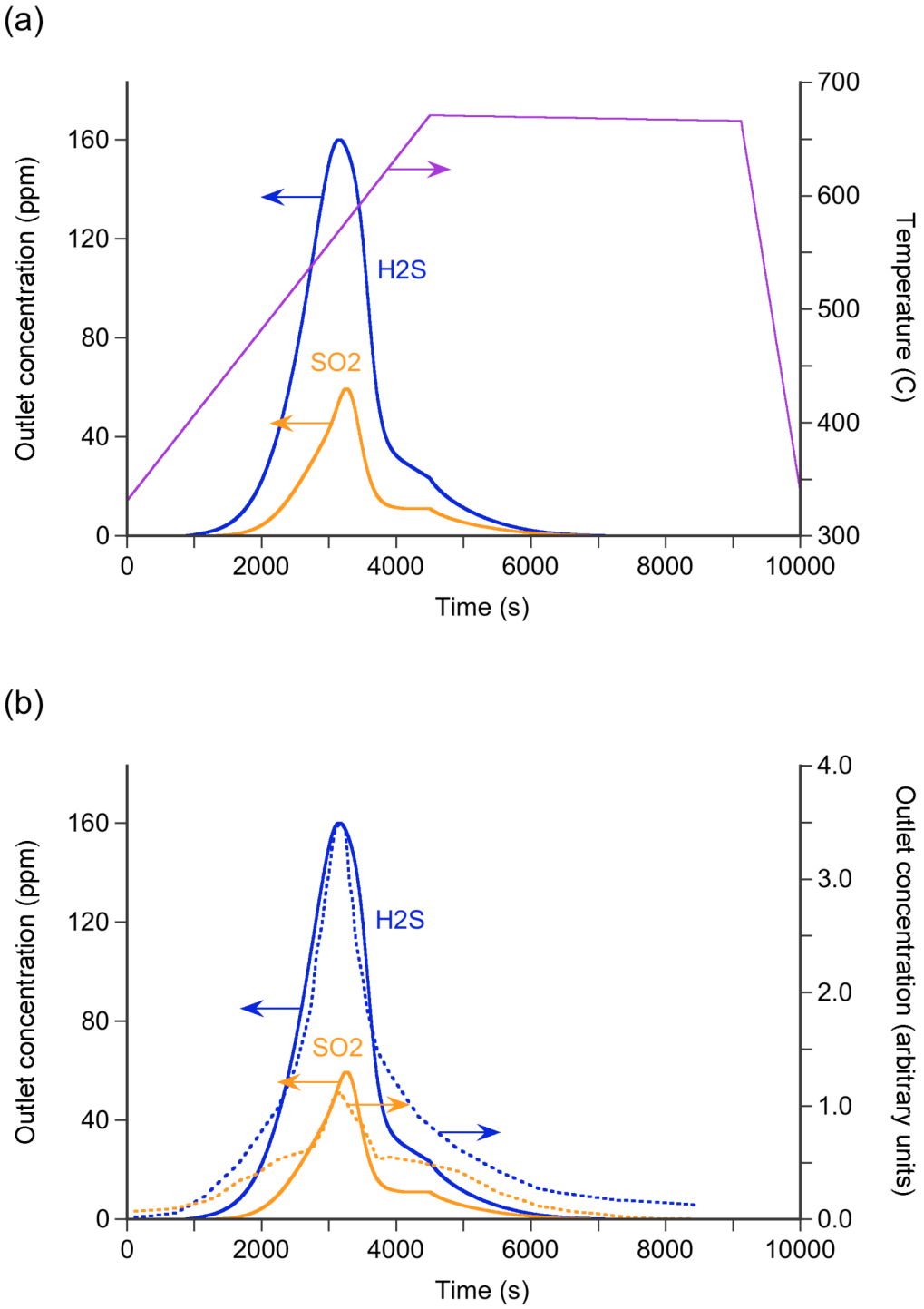

Figure 4. Outlet concentrations of evolved gases during desulfation. (a) simulation results plotted with temperature; (b) simulation results (solid lines) plotted with experimental measurements (dotted lines) from Choi et al. (2007).

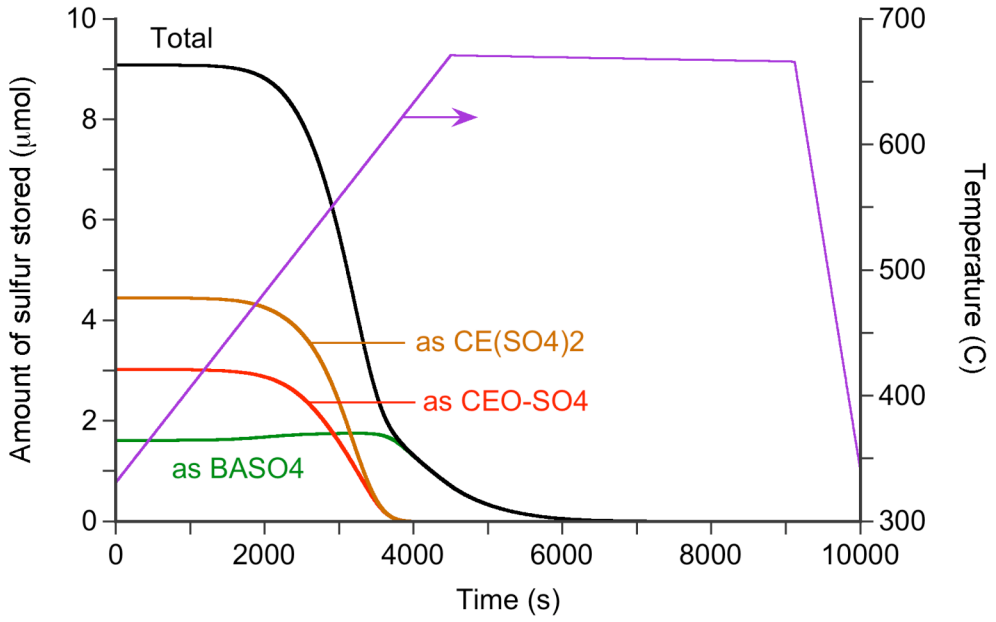

Figure 5. Depletion of individual sulfate species and total trapped sulfur during desulfation.

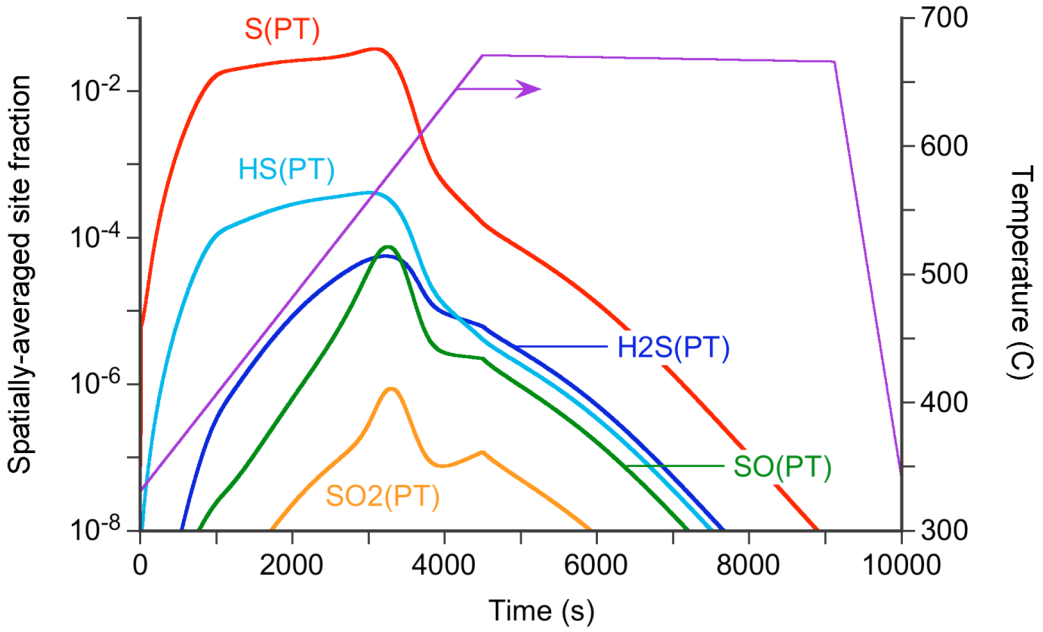

Figure 6. Spatially-averaged concentrations of Pt phase sulfur species during desulfation.

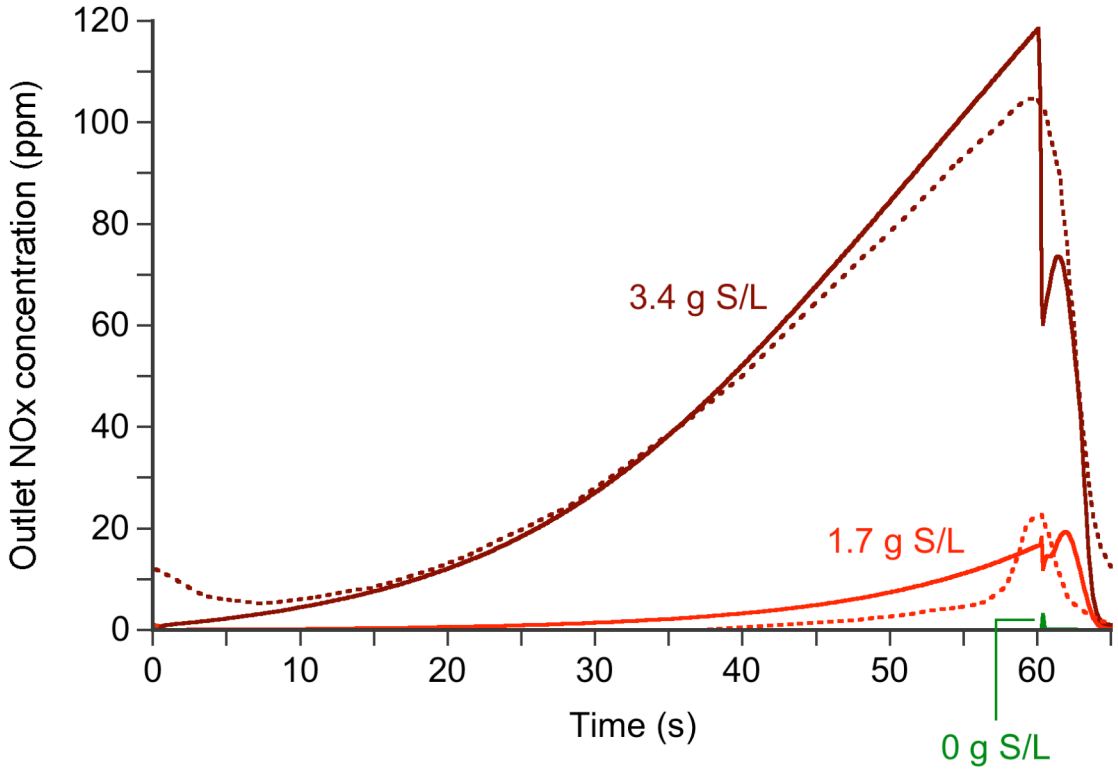

Figure 7. Outlet concentrations of total NO_x during ordinary NSR cycling at various degrees of sulfation. Solid lines are simulation results; dotted lines are experimental measurements from Choi et al. (2007).

6. CONCLUSIONS

We have developed a microkinetic, thermodynamically consistent surface reaction submechanism to account for the sulfation and desulfation behavior of a fully formulated lean NO_x trap. This is appended to a previously developed mechanism for ordinary NO_x storage and reduction (NSR) in order to achieve a more comprehensive modeling tool. A complex test suite consisting of sulfation during rapid cycling, desulfation by temperature-programmed reduction, and periodic NSR performance evaluation has been simulated quite successfully by using the complete mechanism with a transient plug flow reactor code. The simulations describe the reacting flow in a single monolith channel without the use of either gas or solid phase mass transfer resistances. All of the key experimental observations, in particular the nearly complete trapping of inlet SO_2 during normal cycling, the plug-like sulfation of NO_x storage sites, the emission of H_2S and SO_2 during desulfation, and the accelerating effect of sulfation level on NSR performance, are reproduced quite well. In addition, the simulations underscore the vital role played by the oxygen storage sites in preventing the rapid degradation of NO_x storage capacity by sulfation.

REFERENCES

Choi, J.-S., Partridge, W.P., Daw, C.S., 2007. Sulfur impact on NO_x storage, oxygen storage, and ammonia breakthrough during cyclic lean/rich operation of a commercial lean NO_x trap. Applied Catalysis B: Environmental 77, 145–156.

Choi, J.-S., Partridge, W.P., Pihl, J.A., Daw, C.S., 2008. Sulfur and temperature effects on the spatial distribution of reactions inside a lean NO_x trap and resulting changes in global performance. Catalysis Today 136, 173–182.

Choi, J.-S., Partridge, W.P., Lance, M.J., Walker, L.R., Pihl, J.A., Toops, T.J., Finney, C.E.A., Daw, C.S., 2010. Nature and spatial distribution of sulfur species in a sulfated barium-based commercial lean NO_x trap catalyst. Catalysis Today 151, 354–361.

Corbos, E.C., Courtois, X., Bion, N., Marecot, P., Duprez, D., 2008. Impact of the support oxide and Ba loading on the sulfur resistance and regeneration of Pt/Ba/support catalysts. Applied Catalysis B: Environmental 80, 62–71.

Dawody, J., Skoglundh, M., Olsson, L., Fridell, E., 2005. Sulfur deactivation of Pt/SiO_2, $Pt/BaO/Al_2O_3$, and BaO/Al_2O_3 NO_x storage catalysts: Influence of SO_2 exposure conditions. Journal of Catalysis 234, 206–218.

Dawody, J., Skoglundh, M., Olsson, L., Fridell, E., 2007. Kinetic modelling of sulfur deactivation of $Pt/BaO/Al_2O_3$ and BaO/Al_2O_3 NO_x storage catalysts. Applied Catalysis B: Environmental 70, 179–188.

Elbouazzaoui, S., Corbos, E.C., Courtois, X., Marecot, P., Duprez, D., 2005. A study of the deactivation by sulfur and regeneration of a model NSR $Pt/Ba/Al_2O_3$ catalyst. Applied Catalysis B: Environmental 61, 236–243.

Engstrom, P., Amberntsson, A., Skoglundh, M., Fridell, E., Smedler, G., 1999. Sulphur dioxide interaction with NO_x storage catalysts. Applied Catalysis B: Environmental 22, L241–L248.

Griffin, J.D., Kolda, T.G., Lewis, R.M., 2006. Asynchronous parallel generating set search for linearly-constrained optimization. Sandia National Laboratories Report SAND2006-4621.

Han, T., Wu, M.-C., Fisher, G.B., 2005. Computational modeling of diesel NO_x trap desulfation. SAE paper 2005-01-3879.

Happel, M., Desikusumastuti, A., Sobota, M., Laurin, M., Libuda, J., 2010. Impact of sulfur poisoning on the NO_x uptake of a NO_x storage and reduction (NSR) model catalyst. Journal of Physical Chemistry C 114, 4568–4575.

Kee, R.J., Rupley, F.M., Miller, J.A., Coltrin, M.E., Grcar, J.F., Meeks, E., Moffat, H.K., Lutz, A.E., Dixon-Lewis, G., Smooke, M.D., Warnatz, J., Evans, G.H., Larson, R.S., Mitchell, R.E., Petzold, L.R., Reynolds, W.C., Caracotsios, M., Stewart, W.E., Glarborg, P., 1999. CHEMKIN Collection, Release 3.5, Reaction Design, Inc., San Diego, CA.

Kim, D.H., Szanyi, J., Kwak, J.H., Szailer, T., Hanson, J., Wang, C.M., Peden, C.H.F., 2006. Effect of barium loading on the desulfation of Pt-BaO/Al_2O_3 studied by H_2 TPRX, TEM, sulfur K-edge XANES, and in situ TR-XRD. Journal of Physical Chemistry B 110, 10441–10448.

Larson, R.S., Pihl, J.A., Chakravarthy, V.K., Toops, T.J., Daw, C.S., 2008. Microkinetic modeling of lean NO_x trap chemistry under reducing conditions. Catalysis Today 136, 104–120.

Larson, R.S., Chakravarthy, V.K., Pihl, J.A., Daw, C.S., 2011. Simulation of lean NO_x trap performance with microkinetic chemistry and without mass transfer. Sandia National Laboratories Report SAND2011-5575.

Luo, J.-Y., Meng, M., Zha, Y.-Q., Xie, Y.-N., Hu, T.-D., Zhang, J., Liu, T., 2008. A comparative study of $Pt/Ba/Al_2O_3$ and $Pt/Fe-Ba/Al_2O_3$ NSR catalysts: New insights into the interaction of Pt-Ba and the function of Fe. Applied Catalysis B: Environmental 78, 38–52.

Olsson, L., Fredriksson, M., Blint, R.J., 2010. Kinetic modeling of sulfur poisoning and regeneration of lean NO_x traps. Applied Catalysis B: Environmental 100, 31–41.

Roy, S. , Baiker, A., 2009. NO_x storage-reduction catalysis: From mechanism and materials properties to storage-reduction performance. Chemical Reviews 109, 4054–4091.

Sakamoto, Y., Okumura, K., Kizaki, Y., Matsunaga, S., Takahashi, N., Shinjoh, H., 2006. Adsorption and desorption analysis of NO_x and SO_x on a Pt/Ba thin film model catalyst. Journal of Catalysis 238, 361–368.

Sedlmair, C., Seshan, K., Jentys, A., Lercher, J.A., 2002. Studies on the deactivation of NO_x storage-reduction catalysts by sulfur dioxide. Catalysis Today 75, 413–419.

Toops, T.J., Pihl, J.A., 2008. Sulfation of potassium-based lean NO_x trap while cycling between lean and rich conditions — I. Microreactor study. Catalysis Today 136, 164–172.

Wu, M.-C., Han, T., Fisher, G.B., 2005. Experimental evaluation of reformate-assisted diesel NO_x trap desulfation. SAE paper 2005-01-3878.

Appendix A

The five components of the objective function used in optimizing the kinetic parameters were calculated as follows:

(1) Compute the average value of the sum of the exit mole fractions of SO_2, SO_3, and H_2S over all of the sulfation cycles, and multiply the result by 10^4 (an intuitively chosen weighting factor).

(2) Given the axial profile of the $BaSO_4$ site fraction after the last sulfation cycle, find the value in the transition zone that is farthest from either of the two limiting values zero and unity. Then compute the root-mean-square deviation of the remaining values from either unity (for points to the left) or zero (for points to the right). Multiply the result by 0.1. Because there is never a perfectly sharp transition, the "central" transition point cannot by itself indicate a significant deviation from plug-like behavior, so it is not included in the calculation.

(3) At 19 distinct time points during desulfation (separated by 200 s near the peak and 600 s elsewhere), scale the simulated exit concentrations of H_2S and SO_2 by the overall maximum value of either one. Do the same for the experimental results, which are reported in arbitrary units. Then compute the root-mean-square deviation for the 38 pairs of values.

(4) Compute the total amount of stored sulfate (on either BaO or CeO_2) both before and after desulfation, divide the latter by the former, and then divide the result by 15.

(5) For each of four simulated NSR performance evaluation cycles (before sulfation, after 111 sulfation cycles, after 222 sulfation cycles, and after desulfation), compute the time integral of the outlet total NO_x concentration, and express the result in ppm-s. Do the same for the experimental data. Compute the root-mean-square deviation between the four pairs of values, and divide the result by 10^3.

The overall objective function is simply the sum of the five components. The addition of these diverse values is made possible by the weighting factors applied to four of the components, these factors of course being somewhat subjective.

Appendix B

Reactions in the NO_x storage/reduction mechanism and the corresponding kinetic parameters (Larson et al., 2011). An asterisk indicates a core reaction.

No.	Reaction	*A* (cgs units)	*n*	*E* (kJ/mol)
Reactions on precious metal (Pt) sites:				
(S1)*	NO + V(Pt) = NO(Pt)	3.890E+13	0	27.59
		5.818E+12	0	72.82
(S2)*	NO_2 + V(Pt) = NO_2(Pt)	2.248E+10	0	17.97
		1.961E+14	0	100.51
(S3)*	CO + V(Pt) = CO(Pt)	2.594E+21	0	99.99
		1.130E+14	0	99.99
(S4)*	H_2O(Pt) = H_2O + V(Pt)	2.992E+12	0	87.07
		5.071E+13	0	53.83
(S5)*	NH_3 + V(Pt) = NH_3(Pt)	7.574E+30	0	193.14
		1.329E+27	0	193.44
(S6)*	O_2 + 2V(Pt) = 2O(Pt)	4.776E+24	0	58.39
		2.070E+29	0	182.81
(S7)*	H_2 + 2V(Pt) = 2H(Pt)	1.058E+23	0	51.93
		8.436E+21	0	81.06
(S8)	CO(Pt) + O(Pt) = CO_2 + 2V(Pt)	1.073E+13	0	7.54
		4.783E+21	–0.4874	228.90
(S9)	2N(Pt) = N_2 + 2V(Pt)	2.773E+16	0	88.13
		3.587E+11	0.0482	123.47
(S10)	NO(Pt) + NH(Pt) = N_2O(Pt) + H(Pt)	9.373E+11	0.6092	45.87
		2.270E+20	0	41.70
(S11)	2N(Pt) + O(Pt) = N_2O(Pt) + 2V(Pt)	2.102E+32	0	164.37
		1.524E+29	–0.6092	56.44
(S12)*	NO(Pt) + V(Pt) = N(Pt) + O(Pt)	9.392E+18	0	85.01
		1.383E+25	0	174.58

(S13)	$NO(Pt) + O(Pt) = NO_2(Pt) + V(Pt)$	4.862E+25	0.2231	168.59
		1.868E+30	0	200.69
(S14)	$H(Pt) + OH(Pt) = H_2O(Pt) + V(Pt)$	1.945E+20	0	0.82
		6.140E+25	0.6230	160.82
(S15)*	$H(Pt) + O(Pt) = OH(Pt) + V(Pt)$	2.348E+21	0	0.00
		3.379E+11	0	21.03
(S16)	$NH_3(Pt) + V(Pt) = NH_2(Pt) + H(Pt)$	6.057E+18	0.8602	105.34
		3.619E+28	0	142.89
(S17)*	$NH(Pt) + H(Pt) = NH_2(Pt) + V(Pt)$	1.179E+12	0	19.12
		4.772E+20	0	87.26
(S18)*	$N(Pt) + H(Pt) = NH(Pt) + V(Pt)$	9.604E+22	0	89.08
		4.234E+17	0	74.89
(S19)	$NH_3(Pt) + O(Pt) = NH_2(Pt) + OH(Pt)$	3.367E+18	0	33.26
		2.895E+18	–0.8602	91.85
(S20)	$NO(Pt) + H(Pt) = N(Pt) + OH(Pt)$	3.563E+11	0	17.43
		7.548E+07	0	128.03
(S21)	$N_2O(Pt) + H(Pt) = N_2 + OH(Pt) + V(Pt)$	1.976E+28	0	105.34
		5.073E+16	0.6574	269.64
(S22)	$2NO(Pt) = N_2O(Pt) + O(Pt)$	7.201E+20	0	86.38
		1.132E+30	–0.6092	157.59
(S23)	$NO_2(Pt) + CO(Pt) = NO(Pt) + CO_2 + V(Pt)$	5.620E+20	0	87.77
		6.518E+24	–0.2643	277.03
(S24)	$H_2O(Pt) + CO(Pt) = 2H(Pt) + CO_2$	6.396E+18	0	108.42
		6.274E+31	–1.1104	148.75
(S25)*	$N(Pt) + CO = NCO(Pt)$	2.879E+19	0	106.46
		7.933E+13	0	118.75
(S26)	$NCO(Pt) + H_2O(Pt) = NH_2(Pt) + CO_2 + V(Pt)$	7.648E+20	0	96.32
		2.116E+35	–1.1104	178.31
(S27)*	$N_2O + V(Pt) = N_2O(Pt)$	1.976E+11	0	35.90
		7.936E+11	0	35.90

(S28)	$NO(Pt) + NH_2(Pt) = N_2 + H_2O(Pt) + V(Pt)$	1.492E+09	0	6.87
		7.240E+02	0.6712	258.86

Reactions on NO_x storage (BaO) sites:

(S29)*	$CO_2 + BaO = BaCO_3$	3.589E+07	0	20.13
		1.307E+03	0	37.64
(S30)*	$NO_2 + BaO = BaO–NO_2$	1.107E+08	0	0.00
		1.292E+01	0	28.55
(S31)	$BaO + NO_2 = BaO–O + NO$	1.188E+08	0	3.93
		8.343E+11	0.2231	33.14
(S32)*	$NO_2 + BaO–NO_2 = NO + BaO–NO_3$	2.518E+08	0	1.15
		6.599E+11	0	30.71
(S33)*	$NO_2 + BaO–NO_3 = Ba(NO_3)_2$	5.896E+07	0	7.29
		7.727E+00	0	35.93

Pt-BaO spillover reactions:

(S34)*	$BaO + O(Pt) = BaO–O + V(Pt)$	3.577E+13	0	74.88
		1.655E+17	0	98.88
(S35)	$BaO–NO_2 + O(Pt) = BaO–NO_3 + V(Pt)$	2.402E+04	0	0.00
		4.145E+07	–0.2231	24.35
(S36)	$BaO–NO_2 + H(Pt) = BaO + NO + OH(Pt)$	4.538E+08	0	2.31
		8.496E+05	0.2231	0.00
(S37)	$Ba(NO_3)_2 + H(Pt) = BaO–NO_2 + NO_2 + OH(Pt)$	7.627E+10	0	42.01
		4.852E+04	0.2231	10.05
(S38)	$BaO–NO_2 + CO(Pt) = BaO + NO + CO_2 + V(Pt)$	8.718E+12	0	57.36
		5.055E+28	–0.2643	255.38
(S39)	$BaO–NO_3 + CO(Pt) = BaO–NO_2 + CO_2 + V(Pt)$	6.517E+06	0	0.48
		1.683E+12	–0.2643	197.49
(S40)	$Ba(NO_3)_2 + CO(Pt) = BaO–NO_2 + NO_2 + CO_2 + V(Pt)$	4.423E+07	0	19.14
		8.714E+19	–0.2643	187.51
(S41)	$BaO–NO_2 + N(Pt) = BaO–O + N_2O(Pt)$	1.498E+11	0	55.14
		1.439E+24	–0.3861	82.67

(S42)	$BaO–NO_2 + N(Pt) = BaO–O + N_2 + O(Pt)$	3.535E+15	0	98.45
		6.058E+26	0.2713	269.25
(S43)	$BaO–NO_3 + N(Pt) = BaO–O + N_2 + O_2 + V(Pt)$	1.216E+17	0	106.20
		2.786E+20	0.4944	128.23
(S44)	$Ba(NO_3)_2 + N(Pt) = BaO–NO_3 + N_2 + O_2 + V(Pt)$	1.396E+21	0	156.02
		1.063E+24	0.2713	178.31

Pt-Ce_2O_3 spillover reactions:

(S45)*	$O(Pt) + Ce_2O_3 = V(Pt) + 2CeO_2$	2.566E+08	0	19.87
		1.152E+12	0	27.79

Distribution

1	MS 0899	Technical Library, 9536
1	MS 9052	D.E. Dedrick, 8367
1	MS 9052	A.H. McDaniel, 8367
1	MS 9053	D.L. Siebers, 8362
1	MS 9054	A. McIlroy, 8350
1	MS 9054	A.E. Pontau, 8360
1	MS 9409	N.R. Fornaciari, 8365


Sandia National Laboratories